

Shape-memory NiTi with two-dimensional networks of micro-channels

Anselm J. Neurohr, David C. Dunand*

Department of Materials Science and Engineering, Northwestern University, Evanston, IL 60208, USA

ARTICLE INFO

Article history:

Received 25 September 2010

Received in revised form 3 November 2010

Accepted 29 November 2010

Available online 1 December 2010

Keywords:

Porous

Nickel titanium

Nitinol

Shape memory

Space-holder

ABSTRACT

A process was developed for fabricating arrays of micro-channels in shape-memory NiTi for bone implant applications, with a tailorable internal architecture expected to improve biomechanical compatibility and osseointegration. Ni–51.4 at.% Ti with 24–34 vol.% porosity was fabricated by electrochemical dissolution of parallel layers of steel wire meshes embedded within a NiTi matrix during hot pressing of NiTi powders. The resulting NiTi structures exhibit parallel layers of orthogonally interconnected micro-channels with 350–400 μm diameters that exactly replicate the steel meshes. When low-carbon steel wires are used, iron diffuses into the surrounding NiTi during the densification step, creating a Fe-enriched zone near the wires. For high-carbon steel wires, TiC forms at the steel/NiTi interface and inhibits iron diffusion but also depletes some titanium from the adjacent NiTi. In both cases, the NiTi regions near the micro-channels exhibit altered phase transformation characteristics. These NiTi structures with replicated networks of micro-channels have excellent potential as bone implants and scaffolds given: (i) the versatility in channel size, shape, fraction and spatial arrangement; (ii) their low stiffness (15–26 GPa), close to 12–17 GPa for cortical bone; (iii) their high compressive strength (420–600 MPa at 8–9% strain); and (iv) their excellent compressive strain recovery (91–94% of an applied strain of 6%) by a combination of elasticity, superelasticity and the shape-memory effect.

© 2010 Acta Materialia Inc. Published by Elsevier Ltd. All rights reserved.

1. Introduction

Porous metals for implant applications – represented mainly by tantalum, stainless steel, chromium–cobalt, titanium, and nickel titanium (NiTi) [1–3] – have two main advantages over their monolithic counterparts. First, open pores, when ranging from 100 to 600 μm in size, permit bone ingrowth, which improves the long-term fixation of the implant at the bone/implant interface [4,5]. Second, porosity lowers the implant stiffness and thus reduces stress-shielding originating from the large stiffness mismatch existing between bone and implant. Stress-shielding leads to implant failure by causing bone resorption and implant loosening [2]. Of the above bulk metallic implant materials for load-bearing implant applications, NiTi has the lowest Young's modulus (68 GPa [6]) and is thus particularly suitable for reducing stress-shielding. Porous NiTi has previously been fabricated [7,8] with average stiffness values as low as that of cortical bone (12–17 GPa) or even cancellous bone (<3 GPa) [9].

During the initial linear range of the stress–strain curve, NiTi can exhibit an apparent stiffness well below its already low Young's modulus as a result of reorientation of existing twins (for shape-memory martensitic NiTi) or creation of stress-induced twins (for superelastic austenitic NiTi). Further large-scale

twin-mediated deformation can accrue in the stress plateau of NiTi, beyond the macroscopic yield point, with compressive strains of $\sim 4\%$ (well beyond the elastic limit of bone, $\sim 1\text{--}2\%$ [9,10]) that can be recovered completely upon heating (for shape-memory NiTi) or removal of the stress (for superelastic NiTi) [11]. Also, superelasticity delays the onset of plasticity at stress concentrators such as pores [12] and increases the material's energy absorption and damping capacity [13,14]. Finally, the superelastic and shape-memory effects can provide a mechanism for deploying and fixating the implant, similar to NiTi stents and staples [15].

To permit bone ingrowth while retaining low stiffness, high strength, and high superelasticity/shape-memory in porous NiTi, it is important to control the pore size, shape, volume fraction, and connectivity during processing. Fabrication of NiTi foams has to date been performed almost exclusively by the powder metallurgy route, using either elemental or pre-alloyed powders, as reviewed in Ref. [4]. Powder metallurgy techniques used for creating porous NiTi include partial powder sintering [16–25], transient liquid phase sintering [26,27], expansion of argon entrapped during hot isostatic pressing (HIP) of powders [28–31], self-propagating high-temperature synthesis (SHS) [7,32–38], metal injection molding (MIM) followed by sintering or SHS [39,40], and combinations of these techniques with various space-holder materials. Also, laser engineered net shaping (LENS) [41] and selective laser sintering (SLS) [42,43] have recently been employed to fabricate NiTi scaffolds from powders.

* Corresponding author. Tel.: +1 847 491 5370.

E-mail address: dunand@northwestern.edu (D.C. Dunand).

Partial powder sintering produces pores whose size and shape are constrained by the initial powder size. Pore sizes are smaller than the powders and foam strength is often compromised due to the irregular pore shape [16]. Expansion of entrapped argon gas also produces only low porosities due to the high creep strength and low creep ductility of NiTi [29,31]. SHS from elemental powders produces inhomogeneous porosity and allows only limited control over pore characteristics. Furthermore, it often forms intermetallic phases such as Ti_2Ni , Ni_3Ti , and Ni_4Ti_3 that lack the superelastic properties of NiTi and can embrittle the NiTi phase [7,16,37]. LENS and SLS are capable of tailoring pore characteristics closely but often fail to achieve full powder densification, resulting in a significant amount of closed porosity [41–43].

Sintering metallic powders in the presence of a space-holder creates pores whose size, volume fraction and morphology are controlled independently and easily by the space-holder. Temporary space-holders used for NiTi include ammonium bicarbonate [44–46], polymethyl methacrylate [40] and magnesium [47]. Removal of these space-holders occurs by thermal decomposition or evaporation and can thus be integrated into the sintering processing stage. On the other hand, permanent space-holders such as sodium chloride [8,40,48] and sodium fluoride [49] are removed subsequent to high-temperature densification of the NiTi matrix. While permanent space-holders thus require an additional processing step, they prevent pore collapse when powder densification occurs under an externally applied pressure (unlike temporary space-holders that are removed early in the sintering process), thereby allowing more complete NiTi powder densification, e.g., by HIP or hot die pressing.

All previous accounts of NiTi foams created by the space-holder method describe materials with equiaxed pores. However, interconnected elongated pores or micro-channels would more closely mimic the internal pore architecture of bone and could be used to tailor the implant mechanical properties (in particular, stiffness, strength and ductility) by controlling their orientation [50]. Moreover, micro-channels provide unobstructed access for the penetration of bone deep into the implant, unlike fenestrations between rounded pores that can restrict access from one pore to another, as discussed in Ref. [8]. Recent work by Dunand and co-workers [51–53] demonstrated a novel technique for creating metallic foams with elongated, interconnected micro-channels: low-carbon steel wires woven into meshes were used as permanent space-holders in commercially pure titanium and alloyed Ti–6Al–4V and were removed electrochemically after the powder densification step. Iron diffused a few tens of micrometers around the wires into the titanium matrix, and this Fe-rich zone could be removed along with the space-holder to increase the final micro-channel diameter. Conversely, if the steel was first carburized, titanium carbide (TiC) formed at the steel/titanium interface inhibiting Fe diffusion, so that the micro-channels exactly replicated the wire diameter.

In this work, we demonstrate the use of steel wire meshes as space-holders for the fabrication of porous shape-memory NiTi. This technique, which to date has been used only for Ti and Ti–6Al–4V [51–53], permits an unprecedented degree of control over the final pore characteristics in NiTi, enabling for the first time the fabrication of porous NiTi with elongated, aligned, and orthogonally interconnected micro-channels and a fully densified matrix. These porous structures possess a microstructure, phase transformation, and mechanical behavior suitable for load-bearing bone implants.

2. Experimental procedures

2.1. Materials

To avoid compositional fluctuations from the use of elemental powders, pre-alloyed NiTi powders (from Special Metals Corp.,

NY) with a nominal composition of 48.6 at.% Ni and 99.9% purity were used as in previous research [8,27,49]. The powders, which were sieved to a size range of 63–177 μm , are nearly spherical in shape and have a smooth surface and small satellites (Fig. 1a), suggestive of fabrication by liquid spraying.

The space-holders were low-carbon steel wire meshes woven in an orthogonal pattern. Two types of meshes (supplied by McMaster-Carr, Elmhurst, IL) were used, resulting in different final porosities: the first consisted of 356 μm diameter wires spaced 711 μm apart with an open area of 44% (referred to hereafter as “coarse meshes”, Fig. 1b); and the second had 406 μm diameter wires spaced 432 μm apart with an open area of 27% (referred to as “fine meshes”, Fig. 1c). The meshes were embedded in pure carbon powders within steel envelopes and pack-carburized at 960 °C for 2 h. The goal of this operation was to supply enough carbon to the wire so that a TiC surface layer could form at the steel/NiTi interface during hot-pressing to prevent interdiffusion between the two phases, as shown previously for Ti and Ti–6Al–4V [51–53].

2.2. Composite densification

Three composites were made by pouring layers of NiTi powders alternating with meshes (cut into disks with 25 mm diameter) into a 25.4 mm diameter die, resulting in ~ 14 mm tall cylindrical steel/NiTi composites after powder densification. Prior to pressing, the TZM die and pistons were coated with boron nitride to reduce friction. Parallelism of the meshes was ensured by manually compacting and leveling each individual layer of NiTi powders.

For the first NiTi/steel composite, five layers of 3 g of NiTi powders were poured, alternating with four coarse steel meshes. Each mesh has been carburized for a different time: 0, 2, 5, and 9 h. This composite, and the porous specimens created from it, are labeled hereafter as C for “carburization” (since it was used to determine the effect of carbon content).

A second composite was created by pouring 19 layers of 1.74 g of NiTi powders alternating with 18 fine steel meshes previously carburized for 2 h. To achieve in-plane isotropy, the orientation of the meshes was varied in the following order: 0°, –15°, +15°, –30°, +30°, –45°, –38°, +38°, –23°, +23°, –8°, +8°, 0°, –15°, +15°, –30°, +30°, –45°, 0°. This composite and specimens cut from it are labeled HP (for “high porosity”). Likewise for the third composite (called LP, for “low porosity”), 18 layers of 2.1 g of NiTi powders were poured into the die, alternating with 17 coarse meshes oriented in the same isotropic manner. The amounts of NiTi powders between each mesh for the LP and HP composites were chosen such that the distance between the meshes after powder densification was the same ($\sim 50 \mu m$) for both samples. Thus, the final porosities are predicated solely on the wire area density of the two types of meshes used, not on the thickness of dense NiTi between the meshes. Lastly, a monolithic NiTi control sample was made by the same method without steel meshes.

The mesh/powder preforms were densified by hot-pressing at 1020 °C (below the >1100 °C eutectic point in the Fe–Ni–Ti ternary system [54]). For specimen HP, a uniaxial pressure of 40 MPa was applied for 3 h, followed by an additional 3 h at 60 MPa to complete densification. For specimens LP and C and for the monolithic control sample, a pressure of 60 MPa was applied for 3 h. The hot press, which is described in more detail elsewhere [55], was evacuated to 10^{-6} torr residual pressure. Densification was monitored continuously using a displacement transducer and deemed complete when the piston displacement became negligible. The densified composites were then cooled at very low stress (~ 0.5 MPa) to room temperature in vacuum over ~ 3 h.

Several $5 \times 5 \times 10$ mm parallelepipeds were cut from the hot-pressed composites by electric discharge machining (EDM), exposing the steel wires to their surfaces and with their long sides

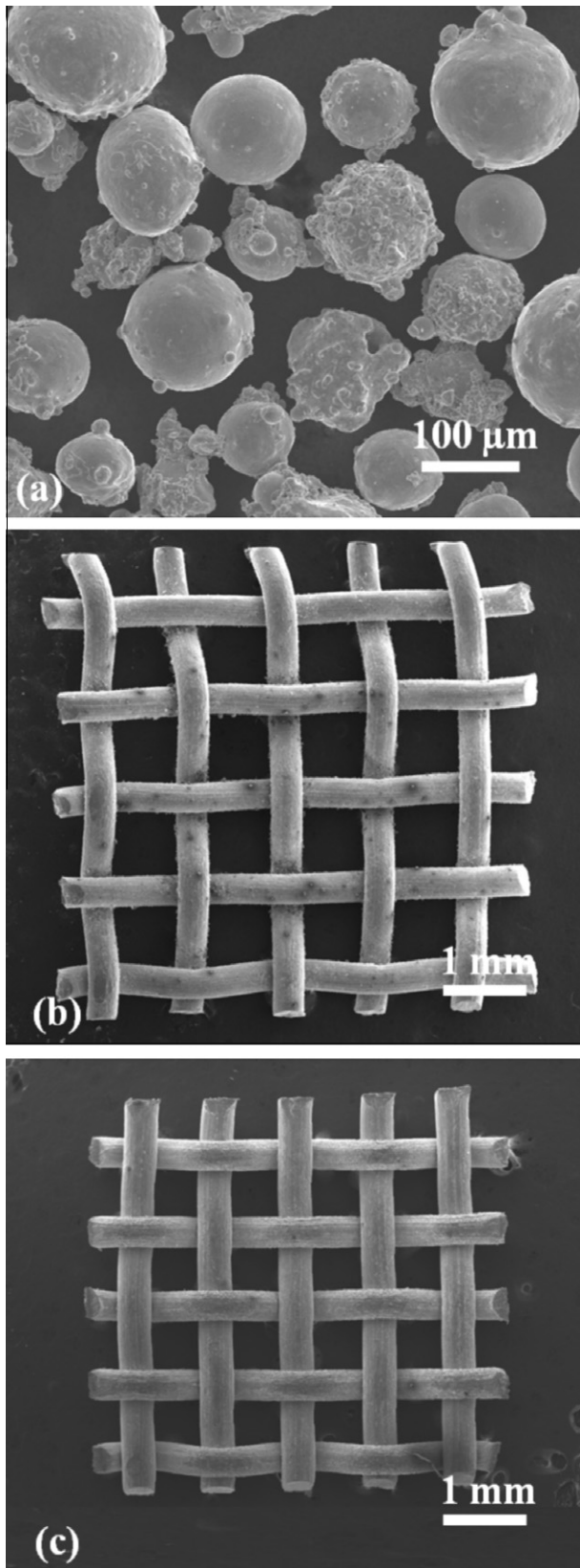


Fig. 1. Scanning electron micrographs of (a) the initial NiTi powders, (b) a coarse steel mesh space-holder, and (c) a fine steel mesh space-holder.

perpendicular to the wire mesh plane (as shown after space-holder removal in Fig. 2).

2.3. Steel dissolution

The steel wires were removed electrochemically from the as-machined steel/NiTi composites. The cathode was a 500 μm thick sheet of commercially pure titanium (CP-Ti) wrapped around the inside of a glass beaker to create a uniform radial potential field. The steel/NiTi composites were attached with nylon wire to a CP-Ti anode and immersed in an electrolyte in the glass beaker. A voltage potential was supplied across the electrodes by a DC power source, allowing for the selective removal of the less noble steel space-holder. The beaker was placed in a sonicator to help remove any loosely adhering iron oxide formed by the electrochemical reaction and to supply fresh electrolyte to the reaction surfaces. Dissolution progress was assessed by periodically measuring the mass loss and comparing to the original mass fraction of steel. Furthermore, discolouration of the NiTi indicated the point when all steel had been removed and the NiTi was no longer cathodically protected from corroding.

Various combinations of electrolytes and voltages were tested on composite C to optimize the space-holder removal. The electrolytes investigated were saturated sodium chloride solutions containing 0–10% acetic acid. The voltage ranged from 0.5 to 1.5 V. The best dissolution results were obtained with an electrolyte containing 3% acetic acid under a voltage of 0.8 V and these parameters were used for space-holder removal in composites LP and HP.

2.4. Microstructural characterization

The carbon contents of the meshes used in specimens C, LP, and HP were measured by wet chemical analysis on ~1 g samples. The iron content of specimens LP and HP after wire dissolution was measured by atomic spectroscopy on ~1.5 g samples. Both analyses were performed by Wah Chang Analytical Laboratory Services (Albany, OR). Scanning electron microscopy (SEM) and optical microscopy (OM) were performed on samples that had been ground with 320 μm grit sand paper and then polished with 9, 3 and 0.5 μm diamond and alumina suspensions. Concentration profiles of Fe, Ti, Ni, and C in the NiTi matrix were measured along a direction perpendicular to the micro-channel wall for samples C, LP, and HP by energy dispersive X-ray (EDX) spectroscopy. The channels of these samples had been infiltrated with epoxy resin to contrast the channel surface. Quantitative composition measurements were made by EDX at a working distance of 10 mm, an accelerating voltage of 15 kV, and a counting time of 300 s, with Ni–51.4 at.% Ti and pure Fe samples used as calibration.

The total porosities of the samples were calculated from mass and volume measurements, using 6.45 g cm^{-3} as the density of NiTi [56]. Closed porosity was measured by helium pycnometry and open porosity was calculated as the difference between total and closed porosity.

The phase transformation behavior was recorded by differential scanning calorimetry (DSC) performed under nitrogen cover gas and at heating/cooling rates of 5 K min^{-1} . The test samples weighed ~20 mg and were cut with a diamond saw. For each sample, two consecutive DSC cycles ranging from -60 to $170 \text{ }^\circ\text{C}$ were performed and the second was used to measure the transformation enthalpies (from the areas under the peaks) and the austenite-start and -finish (A_s and A_f) and martensite-start and -finish (M_s and M_f) temperatures (by extrapolating the intercepts of the tangents of inflection points with the baseline).

2.5. Mechanical properties characterization

Compression testing of the porous samples was performed on a screw-driven load frame with strain calculated from cross-head displacement after correcting for machine compliance. To obtain

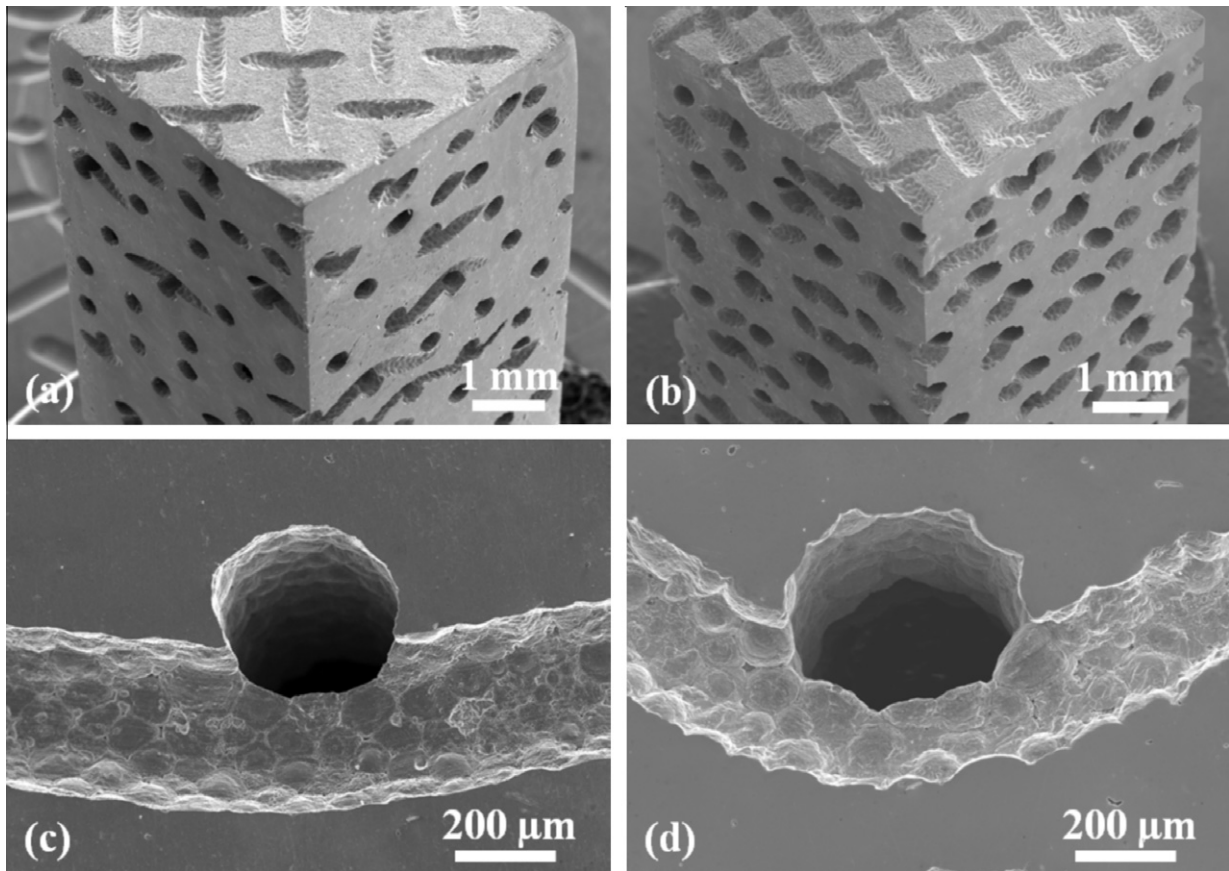


Fig. 2. Scanning electron micrographs of machined compression specimens of (a) sample LP and (b) sample HP. Intersections between two orthogonal micro-channels are shown at higher magnification for (c) sample LP and (d) sample HP.

accurate stiffness measurements, an extensometer attached directly to the samples was used at strains up to $\sim 5\%$. To assure parallelism, an alignment cage was used. Prior to mechanical testing, the specimens were polished with 600 μm grit sandpaper to remove any surface oxides formed during the EDM process. To ensure that the samples have a fully martensitic microstructure, they were annealed for 15 min at 130 $^{\circ}\text{C}$ in air, cooled to and maintained at room temperature for 20 min, immersed in liquid nitrogen for 3 min, and warmed to and maintained at room temperature for 20 min.

A first set of samples (HP and LP) was subjected to a series of load–unload–recovery cycles at a cross-head speed of 0.05 mm min^{-1} . The specimens were deformed in uniaxial compression at ambient temperature to a maximum strain of ε_{max} , then unloaded, removed from the cage, and heat-treated as before the test. The specimen dimensions were measured before loading, after unloading, and after the subsequent shape-memory recovery heat-treatment. The load–unload–recovery cycles were repeated several times with ε_{max} starting at 1% and increasing by 1% for each consecutive cycle until a load drop was observed. Monotonic compression tests were performed on a second set of samples (HP, LP and control) at a cross-head speed of 0.15 mm min^{-1} , where the specimens were loaded until failure occurred.

3. Results

3.1. Mesh carburization

Table 1 shows the carbon contents of the four meshes used in sample C along with the meshes used in samples LP and HP. The

carburization was successful for meshes used for sample LP but not for those used in sample HP, as further evidenced by a lack of TiC formation at the micro-channel walls in that sample. Furthermore, sample HP showed a significantly higher average iron content (1.22 wt.%) than sample LP (0.14 wt.%).

In sample C, no difference was observed in the EDX profiles for meshes carburized for 2, 5, or 9 h, so the 2 h carburization time was chosen for the meshes used in samples LP and HP. Fig. 2 shows that, for both carburized and uncarburized meshes (samples LP and HP), the final micro-channel diameter was the same as that of the initial steel wire. Fig. 3a plots the Fe, Ti, and Ni concentrations in the NiTi matrix next to a carburized mesh (as in sample LP), showing a Ti peak at the channel wall and effectively no Fe in the NiTi matrix. The C profiles are omitted in Fig. 3 because they are distorted by C signals emanating from the epoxy resin in the channels. However, C peaks were clearly visible at the steel/NiTi interface before dissolution of the carburized meshes. The Ti and C peaks indicate that a layer of titanium carbide (TiC, which is the only compound in the Ti–C system [57]) formed at the wire

Table 1

Carbon contents of the steel meshes, and resulting TiC formation in the corresponding steel/NiTi composites.

Mesh type	Specimen	Carbon content (wt.%)	TiC layer
Coarse	C	0.063	No
Coarse	C	0.370	Yes
Coarse	C	0.410	Yes
Coarse	C	0.820	Yes
Coarse	LP	0.600	Yes
Fine	HP	0.052	No

surface, which is also visible by optical microscopy (inset of Fig. 3a), and prevented the diffusion of Fe into the NiTi, as previously observed in Ti [51] and Ti–6Al–4V [52]. No such peaks were observed at micro-channels produced from uncarburized meshes (as in sample HP, Fig. 3b) and Fe diffused into the NiTi matrix to a distance of $\sim 40 \mu\text{m}$. The arrows in the inset optical micrographs in Fig. 3a and b show the approximate locations of the line scans and are marked to indicate the positions of the individual quantitative analyses shown in Fig. 3c and d.

Fig. 3c shows the Ni content (from quantitative EDX measurements with an estimated error of $\pm 0.2 \text{ at.}\%$) in sample LP as a function of distance from the channel wall. The TiC layer is $\sim 7 \mu\text{m}$ thick (from Fig. 3a) and surrounded by $\sim 40 \mu\text{m}$ of Ni-rich NiTi due to Ti depletion, which results from Ti consumption by the adjacent TiC region. The TiC coats the channel walls, thus preventing any potential Ni leaching. The widths of the data points indicate the approximate beam diameter and emphasize that the measurements are averages over a spot with $\sim 8 \mu\text{m}$ diameter. In Fig. 3d, the Fe and Ni compositions (from quantitative EDX measurements) in sample HP produced with uncarburized meshes are plotted together with a Fe line scan (from Fig. 3b), showing that Fe replaces Ni in the NiTi lattice, as previously documented in bulk NiTi [58,59]. Thus the (Ni, Fe)Ti material adjacent to the channel wall is Ni depleted as compared to the original NiTi. (Ni, Fe)Ti near the micro-channels containing $>5.7 \text{ at.}\%$ Fe does not transform within the temperature range of the DSC cycle ($-60 \text{ }^\circ\text{C}$ to $170 \text{ }^\circ\text{C}$) [60]. As the Fe content decreases farther from the channels, (Ni, Fe)Ti will only partially transform within these temperatures via the two-step

B2 \rightarrow R \rightarrow B19' transformation because the M_s temperature (corresponding to the R \rightarrow B19' peak) quickly drops below $-60 \text{ }^\circ\text{C}$ [60,61]. As illustrated in Fig. 3d, the thickness of the non-transforming layer is $\sim 11 \mu\text{m}$, surrounded by $\sim 29 \mu\text{m}$ of partially transforming (Ni, Fe)Ti with $<5.7 \text{ at.}\%$ Fe.

Since the formation of TiC results in Ti-depletion in the adjacent material, it is expected that the Ni-content be highest at the TiC/NiTi interface [62] (indicated by the left vertical dashed line in Fig. 3c). Similarly a maximum in the Fe content is expected at the channel wall (located at the origin in Fig. 3d). As the EDX measurements are inaccurate near the interface because of the finite width of the electron beam, expected trends are shown as dotted gray lines in Fig. 3c and d.

3.2. Mesh removal and micro-channel morphology

Acetic acid was shown to be more effective than other common acids in experiments done on CP-Ti containing embedded steel wires [51]. In the present study of NiTi, it was also found that the addition of acetic acid to the sodium chloride solution (which was used previously for Ti–6Al–4V [52]) accelerated the dissolution of the steel. The optimal dissolution parameters were found to be an electrolyte consisting of 3% acetic acid in a saturated sodium chloride aqueous solution and a voltage of 0.8 V. In general, increasing the voltage and/or acid content resulted in pitting corrosion of the NiTi matrix, while reducing the voltage slowed the reaction kinetics. Reducing the acid content below 3% resulted in the deposition of iron oxide on the NiTi surface. Using these

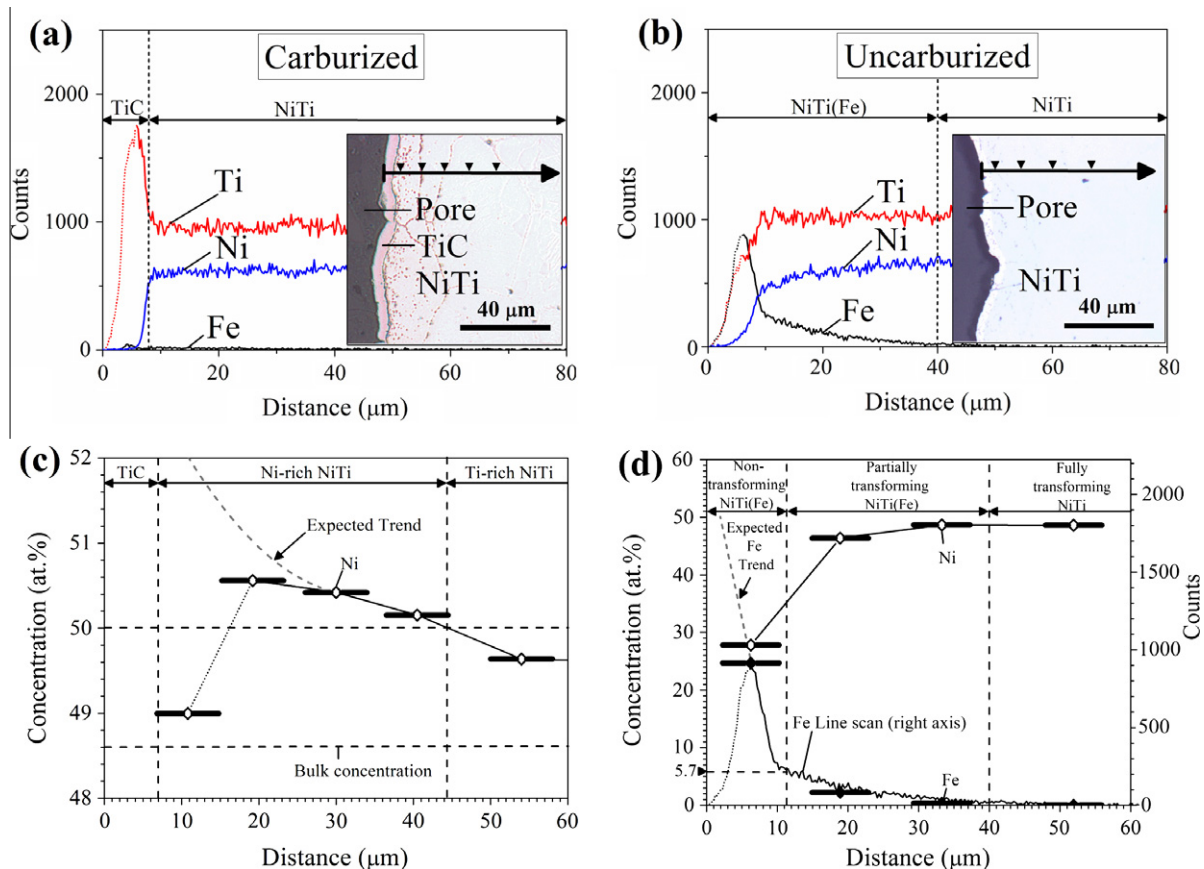


Fig. 3. EDX line scans across the NiTi matrix starting at the walls of micro-channels created by (a) a carburized steel wire (sample C) and (b) an uncarburized steel wire (sample C). (c) Nickel concentration profile in sample LP measured by quantitative EDX. (d) Iron and nickel concentration profiles in sample HP measured by quantitative EDX, with the iron line scan (shown in (b)) superimposed. The width of the data points in (c) and (d) corresponds to the approximate beam width. The origins of all graphs are at the micro-channel walls. The arrows in the inset optical micrographs of cross-sections of the channel/matrix interfaces in (a) and (b) illustrate representative locations and directions of the line scans and are marked with the locations of the quantitative EDX measurements.

parameters, the steel dissolution in $5 \times 5 \times 10$ mm samples of composites LP and HP was complete after ~ 25 – 35 h.

Samples LP and HP have an average total porosity of $23.7 \pm 0.3\%$ ($23.3 \pm 0.3\%$ open porosity) and $33.5 \pm 0.1\%$ ($33.4 \pm 0.1\%$ open porosity), respectively. Expected open porosities of the samples were calculated from the physical parameters of the space-holder meshes. The calculated values (23.6% and 30.3%) match the experimentally measured porosities (23.3% and 33.4%, respectively). Small differences may arise due to powder losses while assembling the preform.

The monolithic control sample has a closed porosity of $0.2 \pm 0.1\%$. Thus, there is near-zero closed porosity, as confirmed by Fig. 2a–d, which depicts a fully densified NiTi matrix. These figures illustrate that the networks of channels faithfully replicate the steel meshes (shown in Fig. 1b and c). The channels extend throughout the sample and are interconnected in two directions (i.e., in the planes of the individual meshes). Fig. 2c and d shows the intersections between two orthogonal channels, illustrating that the fenestration connecting them has a size comparable to the channel diameter. The micro-channels in both samples have a dimpled surface resulting from the indentation of the steel wires by the NiTi powders during hot-pressing.

3.3. Phase transformations

DSC thermograms of samples LP and HP, the initial NiTi powders, and the monolithic NiTi control sample are displayed in Fig. 4. The NiTi powders show a secondary peak overlapping slightly with the primary peak, indicating the presence of an intermediate R-phase. All other samples (LP, HP and the control) show a single peak during heating and cooling, most probably because of the annealing occurring during the hot pressing operation [63], so that the transformation from the austenite to the martensite

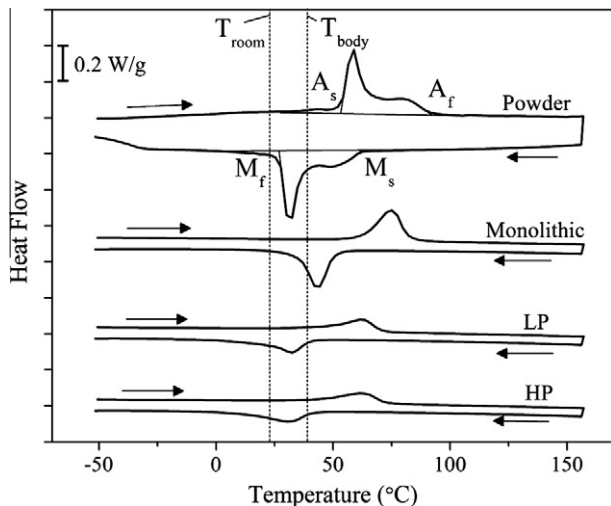


Fig. 4. DSC thermograms of the as-received NiTi powder, monolithic control sample, and samples LP and HP. The vertical dashed lines indicate room and body temperatures.

phase occurs in a single step. Table 2 summarizes the transformation enthalpies and temperatures of each sample, along with the austenitic and martensitic transformation intervals (A_f – A_s and M_s – M_f , respectively) and the peak-to-peak hysteresis (A_p – M_p). The porous specimens differ from the monolithic control specimen in the following: (i) lower transformation enthalpies; (ii) decreased transformation temperatures; and (iii) broader martensitic and, to a lesser extent, austenitic transformation intervals. Sample HP has slightly lower enthalpies and broader austenitic and martensitic transformation intervals than sample LP.

3.4. Compressive and shape-memory properties

Compressive stress–strain curves for samples LP and HP tested under monotonic loading conditions are shown in Fig. 5. Sample LP reaches a stress of 600 MPa at a strain of 9% before the stress drops. For sample HP, these values are 420 MPa and 8%, respectively. Both samples exhibit a region between ~ 100 and ~ 250 MPa over which the slope is reduced. Fig. 6 shows the load–unload–recovery cycles for samples LP and HP, with curves shifted along the x-axis for clarity. Sample LP showed a stress drop during the seventh cycle after $\sim 6.5\%$ strain, while sample HP underwent five cycles before damage in the sixth cycle at $\sim 6\%$ strain led to a stress drop.

The load–unload–recovery cycles were used to determine loading stiffness, unloading stiffness, elastic recovery strain (ϵ_{el}), super-elastic recovery strain (ϵ_{se}), thermal recovery strain (ϵ_{rec}), and residual plastic strain (ϵ_{pl}) as a function of the maximum applied strain (ϵ_{max}), with $\epsilon_{max} = \epsilon_{el} + \epsilon_{se} + \epsilon_{rec} + \epsilon_{pl}$. For each strain cycle, the x-intercept of the linear extension of the unloading elastic regime (described in the next paragraph) was found. The distance between this point and the maximum strain is the elastic strain, while the difference between this point and the strain after

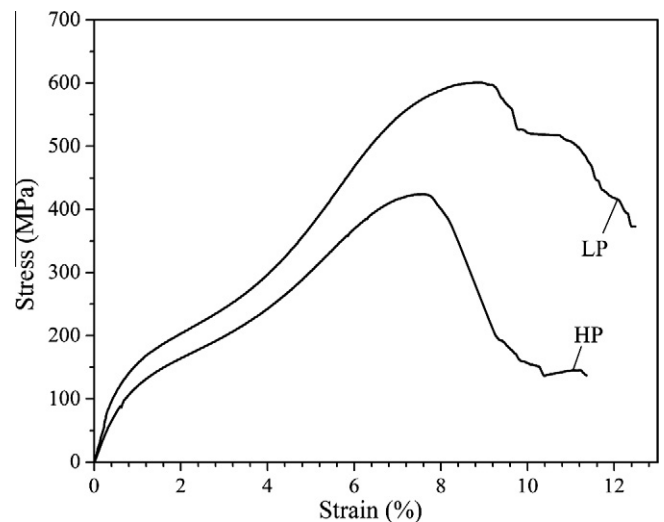


Fig. 5. Compressive stress–strain curves of samples LP and HP under monotonic loading.

Table 2
Phase transformation parameters of NiTi specimens and powders.

Specimen	Enthalpy (J g^{-1})		Transformation temperatures ($^{\circ}\text{C}$)				Transformation intervals ($^{\circ}\text{C}$)		
	Heating	Cooling	A_s	A_f	M_s	M_f	A_p – M_p	A_f – A_s	M_s – M_f
Powder	24 ± 0.1	23 ± 0.7	54 ± 0.3	90 ± 0.5	61 ± 0.4	28 ± 0.3	26 ± 0.5	37 ± 0.6	33 ± 0.5
Monolithic	24 ± 0.8	24 ± 1.1	65 ± 1.7	86 ± 1.4	53 ± 1.4	36 ± 0.6	33 ± 2.4	21 ± 2.2	16 ± 1.5
LP	17 ± 0.9	16 ± 1.1	46 ± 3.0	69 ± 2.1	39 ± 1.7	18 ± 3.1	30 ± 2.6	23 ± 3.7	21 ± 3.5
HP	15 ± 0.5	15 ± 0.5	43 ± 2.4	73 ± 1.8	41 ± 1.1	10 ± 1.7	31 ± 4.6	30 ± 3.0	32 ± 2.1

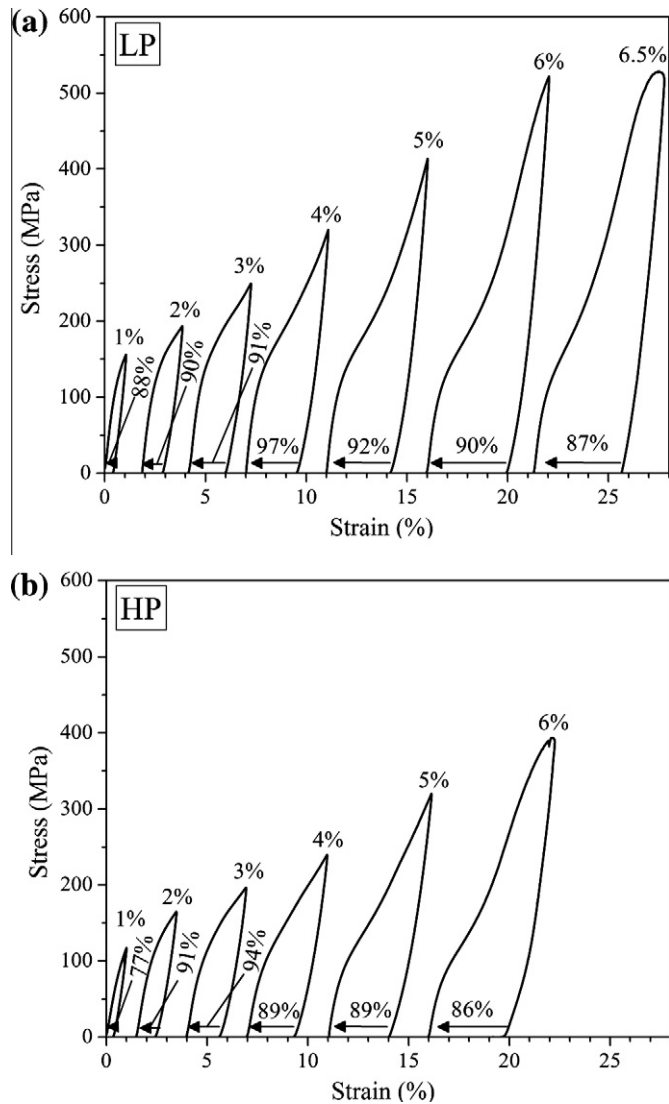


Fig. 6. Compressive stress–strain curves during load–unload–recovery cycles of (a) sample LP and (b) sample HP. The individual cycles are shifted along the *x*-axis for clarity. The numbers above each cycle indicate the maximum applied strain, while the arrows at the bottom of each cycle refer to the fraction of strain recovery during the annealing treatment (with respect to the plastic strain remaining after unloading).

unloading (but before annealing) is the superelastic strain. The thermal strain recovery was determined from the difference in sample height before and after the 130 °C anneal. Similarly, the residual plastic strain was calculated from the difference in sample height prior to compression testing and after annealing. Strain recovery due to the shape-memory effect was observed for each cycle and was in the range 87–97% of the residual plastic strain for sample LP and 77–94% for sample HP (shown in Fig. 6). Fig. 7 depicts the various components of the maximum applied strain and shows that the elastic and superelastic recoveries, which combined make up the strain recovered upon unloading, are significantly lower than the thermal recovery at high applied strains. At low applied strains, however, the unloading recovery (sum of elastic and superelastic strains) is larger than the thermal recovery. The residual plastic strain remains negligible up to 4% applied strain, increasing slowly for higher strains.

The loading stiffness was determined from the slope of a best fit line in the stress range 20–40 MPa, below which sample settling effects may occur, and above which non-linearity can appear. This range of stress values contains the inflection point between

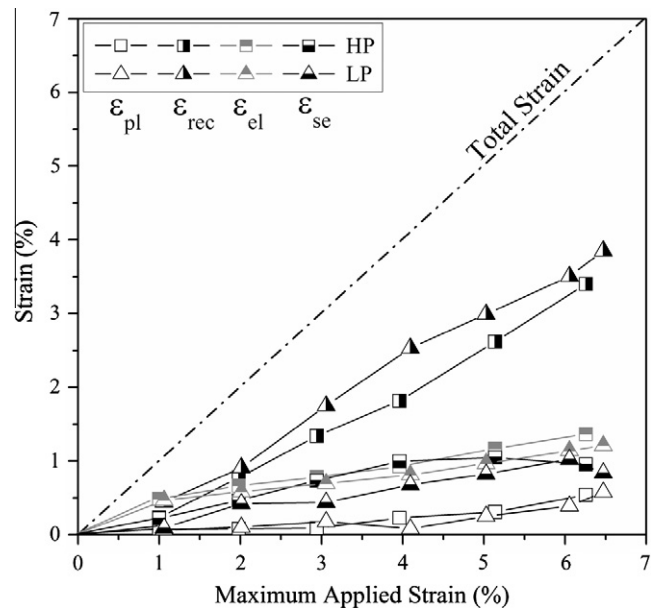


Fig. 7. Plots of elastic recovery strain (ϵ_{el}), superelastic recovery strain (ϵ_{se}), thermal recovery strain (ϵ_{rec}), and residual plastic strain (ϵ_{pl}) as a function of maximum applied strain for samples LP and HP.

concavity (due to settling effects below 20 MPa) and convexity (due to the onset of stress-induced detwinning at stresses above ~40 MPa) and thus represents the portion of the stress–strain curve with the highest slope. Even in this narrow range, detwinning and possibly plastic deformation at stress concentrations may contribute to the measured strain, so the stress/strain slope is not a true Young’s modulus but rather an effective stiffness. The unloading stiffness was measured in a similar fashion. All unloading stresses above $\sigma_{max} - 10$ MPa were ignored to avoid the small stress drop upon unloading due to machine mechanical hysteresis. Again, a 20 MPa interval was used to determine the stiffness from the slope of a best-fit line and stresses below $\sigma_{max} - 30$ MPa were not used. The error associated with these stiffness

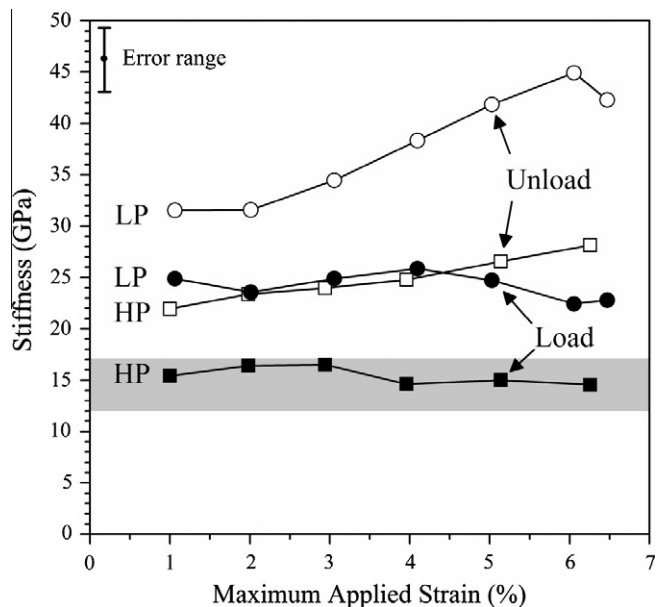


Fig. 8. Plots of loading and unloading stiffness values as a function of maximum applied strain for samples LP and HP. The shaded region shows the range of stiffness values for cortical bone [9].

measurements is relatively large, and is estimated to be ± 3 GPa. Fig. 8 shows the loading and unloading stiffness as a function of the maximum applied strain, for each of the load–unload–recovery loops. For both samples, the loading stiffness stays fairly constant regardless of the prestrain that has been applied. Sample LP exhibits a loading stiffness that is ~ 6 – 11 GPa greater than that of sample HP. The unloading stiffness of both samples increases steadily with maximum applied strain, and is higher than the loading stiffness by ~ 5 – 20 GPa. Lastly, the loading stiffness of the monolithic sample was measured to be 65 GPa from a best-fit line in the same range of stress values (20–40 MPa) as for the other specimens. This value is within error of previous measurements reported for martensitic NiTi (68 ± 5 GPa [6]).

Since twin motion and creation upon loading can reduce the apparent stiffness of NiTi foams in the linear range of the stress–strain curve, attempts were made at measuring the true Young's modulus ultrasonically using 5 MHz contact transducers. Due to the transversely isotropic pore architecture, measurements were needed along principal and non-principal directions. However, these tests were unsuccessful because wave scattering from the large channels was too strong, making it impossible to distinguish the signal peaks along non-principal directions.

4. Discussion

4.1. Processing method

The use of steel space-holders, as compared to the other temporary or permanent space-holders previously used for NiTi (i.e., ammonium bicarbonate [44–46], polymethyl methacrylate [40], saccharose [40], sodium chloride [8,40,48], sodium fluoride [49] and magnesium [47], as reviewed earlier) is motivated by several factors. First, steel is inexpensive and can be very easily formed into ductile wires of various diameters and cross-sectional shapes that can be woven into meshes; this allows for easy tailoring of the pore (or micro-channel) fraction, size, shape, orientation and connectivity. Second, steel has a sufficiently high melting point ($T_m = 1370$ °C) to remain in the solid state during densification by hot-pressing of NiTi powders, so that the space-holder shape is retained during pressure densification. Third, a mechanism for externally driven removal of the space-holder (rather than equilibrium dissolution or evaporation) exists that relies on the different electrochemical responses of steel, which actively dissolves, and NiTi, which forms a passivating oxide layer, when in contact with each other. Fourth, diffusion of Fe in NiTi is slow enough that Fe contamination of the NiTi matrix is localized (Fig. 3b and d). While such contamination may in fact be tolerated up to ~ 6 wt.% without disappearance of the shape-memory effect [60] and may even be desirable to create some (Ni, Fe)Ti superelastic regions around the micro-channels, it can be fully inhibited by carburizing the steel so it forms a protective TiC layer when in contact with NiTi (Fig. 3a), albeit with a local decrease in Ti concentration. The latter decrease could be eliminated by depositing a TiC (or other non-reactive ceramic) on the wires prior to densification with NiTi powders.

To date, only two methods have been shown to produce elongated pores in NiTi. The first is SHS from elemental Ni and Ti powders, which forms channels in the direction of the propagating wave [35]; however, in addition to the drawbacks of SHS mentioned earlier, it is also difficult to control the pore characteristics, in particular interconnectivity. The continuous zone melting technique has also been successful in producing elongated pores in NiTi [64]. Here, hydrogen gas is first dissolved under high pressure into a NiTi melt and, during directional solidification, is rejected at the solid/liquid interface to form cylindrical pores aligned in the

solidification direction. Control over pore size and volume fraction is achieved by altering the hydrogen partial pressure but is more limited than for the space-holder technique; pore orientation is dictated by the solidification gradient and cannot achieve complex structures such as the orthogonal arrays of micro-channels demonstrated here. Finally, the use of hydrogen gas under high pressure and elevated temperature creates safety issues. Compared to the fabrication of NiTi scaffolds by LENS [41] and SLS [42], which allow high control over the cellular architecture by utilizing computer-aided design (CAD) to construct an object layer-by-layer, the present technique presents the advantage of being much simpler and inherently parallel, with micro-channels created simultaneously from all directions during steel dissolution. Moreover, eliminating closed porosity within the NiTi struts remains a challenge in LENS and SLS due to incomplete sintering of the NiTi powders. In the present technique, closed porosity is eliminated and full densification is achieved by applying pressure during the high-temperature sintering. A disadvantage of the present technique compared to SHS, continuous zone melting, LENS, and SLS is the higher number of processing steps involved.

4.2. Effect of mesh carburization

Table 1 shows that the steel carbon content necessary for the formation of TiC lies between 0.06 and 0.37 wt.%. As previously demonstrated for steel wires embedded in CP-Ti [51] and Ti-6Al-4V [52], formation of a TiC layer at the steel/NiTi interface prevented iron from diffusing into the NiTi. All three carburized steel meshes in sample C produced TiC interfacial layers with a thickness of ~ 7 μm (as shown in the inset of Fig. 3a) regardless of carbon content. The effects of TiC on the biocompatibility of NiTi have not yet been assessed, but improved osseointegration has been reported when TiC was present at the surface of titanium substrates [65]. Also, presence of TiC particles within NiTi does not affect significantly its shape-memory or superelastic properties [66,67].

The effects of using uncarburized steel meshes were quite different for NiTi than for CP-Ti [51] or Ti-6Al-4V [52]. In the latter two alloys, the iron-rich diffusion region surrounding the steel wires is removed during the electrochemical dissolution, so that the final micro-channel diameter can be tailored by controlling the amount of iron allowed to diffuse into the matrix. In NiTi, however, the final micro-channel size matches the initial wire diameter regardless of the amount of carburization, and the iron-containing region is not dissolved.

The high iron content in sample HP and the absence of a TiC layer at the channel wall agree with the low carbon content of the meshes (whose carburization was unsuccessful). The average iron content of sample HP is only 1.22 wt.%, but the much higher levels of iron in the (Ni, Fe)Ti layer surrounding the micro-channels (Fig. 3d) depress the transformation temperatures locally (i.e., reducing M_s by 50 K per at.% Fe [13]), as further discussed in the context of the phase transformation and shape-memory behavior in Section 4.4.

4.3. Microstructure

The interweaving and elongated porosity in the NiTi matrix (Fig. 2) indicate that the shape of the meshes (Fig. 1a) is well replicated. The channel diameters are within the optimal size range for bone ingrowth (100–600 μm [4]) throughout the entire thickness of the sample and show none of the constrictions associated with fenestrations between equiaxed pores. Since the steel meshes were permanent, rather than temporary, space-holders, collapse of the porosity did not occur during the hot-pressing operation. However, a dimpled channel surface was created by the indentation of the steel wire by individual NiTi powders (Fig. 2c and d). This

dimpling is exhibited by both LP and HP samples but is more pronounced in the latter, which does not display a hard TiC layer at the wire surface. Previous research has demonstrated a positive correlation between surface roughness and bone integration in titanium implants for roughness values up to 50 μm [68], as well as between surface roughness and osteoblast proliferation, differentiation, and matrix production for roughness values up to 20 μm [69]. The indentations on the channel walls of the present specimens may thus improve implant fixation by stimulating bone growth and providing stronger mechanical anchorage with the bone.

Closed porosity is negligible due to the application of high uniaxial pressure (60 MPa), which progressively becomes quasi-isostatic as densification progresses during the 3 h at 1020 °C. Elimination of microporosity between the NiTi powders, which is necessary for achieving high static and cyclic strengths, is significantly better than in foams created by pressureless sintering at similar temperatures and times [16]. Furthermore, for higher wire contents than those used here, the NiTi walls between micro-channels will become thinner and full powder consolidation more critical to avoid channel collapse after wire removal. The present method has the potential to fabricate foams with much higher porosities than the current value of 34% (i.e., >50%, depending on the arrangement of wires) with thin matrix walls that are fully densified. Near-net shape hot-pressing of implants with complex geometries may also be possible by using shaped dies, provided that the steel wires are allowed to protrude to the surface so they can be electrochemically removed without machining the surface.

The present specimens have a greater surface area than monolithic NiTi, and this is known to increase the amount of Ni release [4]. The extent of leaching of Ni, which is cytotoxic, from the surfaces of NiTi implants remains a controversial issue [70,71], and several surface modifications exist to reduce this effect [4]. However, this effect is not expected to be significant in the present specimens because their specific surface area is smaller, by a factor of >4, than that of the commercially available porous NiTi spinal fusion device called Actipore™ (Biorhex Inc., Montreal, QC, Canada) [72]. Extensive *in vitro* and *in vivo* tests have been performed on these uncoated high-porosity NiTi foams and the results clearly indicated that they are non-sensitizing, non-irritant, non-toxic [73,74] and fully cytocompatible and genocompatible [75,76]. High bone ingrowth and strong bone/implant fixation into NiTi foams were further demonstrated *in vivo* in rabbits [77] and rats [78]. Other researchers have demonstrated in a six week study on rabbits that no adverse reaction occurred from porous NiTi implants, and that the ingrown bone was very similar to the surrounding bone [7].

Moreover, the presence of Ni-depleted regions at the channel surfaces in both specimens LP (due to the TiC layer) and HP (due to the (Ni, Fe)Ti layer, where Fe replaces Ni) may help to decrease the amount of Ni released from the channel surfaces. To understand the effects of the Ni-rich region adjacent to the TiC layer on the Ni release rate in specimen LP, additional experiments are required in the future. Ni-enrichment, which results from the migration of Ti to the adjacent TiC layer, can be prevented by coating the steel meshes with TiC prior to hot-pressing, rather than carburizing them. By this method, no Ti is removed from the adjacent NiTi matrix to form TiC.

4.4. Phase transformation behavior

As shown in Fig. 4, both samples are martensitic at room and body temperatures so that shape-memory behavior is expected. In sample HP, the increased iron content in NiTi leads to a depression of the transformation temperatures [59,63] in the regions surrounding the channels. In sample LP the same result is expected, as carbon consumes titanium to form TiC, thereby increasing the Ni/Ti

ratio and decreasing the transformation temperatures [63,79]. The Fe concentration gradients in sample HP (shown in Fig. 3d) lead to a broadening of the transformation peaks, since the Fe-rich regions in the sample transform at lower temperatures than those with low or no Fe. The TiC in sample LP also leads to slight peak broadening because of local Ni concentration gradients [62], though to a lesser extent than in sample HP. While the formation of TiC and the concomitant consumption of Ti close to the channel wall is inconsequential in unalloyed Ti [51] and Ti-6Al-4V [52], it significantly affects the phase transformation behavior of NiTi, as seen by comparing the transformation temperatures and intervals of sample LP and the monolithic control (Table 2).

By approximating the channels as straight cylinders and referring to Fig. 3c, the volume fractions of TiC and Ni-rich NiTi in the solid matrix of sample LP are calculated to be ~2% and ~16%, respectively. The enthalpy of transformation of sample LP is calculated to be 23 J g⁻¹ from an average enthalpy for the Ni-rich region (between 18 and 24 J g⁻¹ from Ref. [80]) and using an enthalpy of 24.3 J g⁻¹ for the remaining volume of bulk Ti-rich NiTi [56]. Thus the increased Ni-content around the TiC layer should not have a large effect on the enthalpy. Similarly, the volume fractions of non-transforming and partially transforming (Ni, Fe)Ti regions in the solid matrix of sample HP are calculated as ~7% and ~21%, respectively. The total enthalpy of sample HP is then calculated as 20 J g⁻¹, using enthalpy values listed for various (Ni, Fe)Ti alloys in Refs. [60,61,79]. Both calculated enthalpies are significantly higher than those measured by DSC (listed in Table 2), which is probably due to the difficulty in accurately determining the baseline for calculating the areas of the broadened peak.

4.5. Thermo-mechanical properties

4.5.1. Maximum strength

The maximum compressive strength and strain of sample HP with 34% porosity (420 MPa at 7.6% strain, Fig. 5) are higher than those reported for a martensitic NiTi foam with 36% uniformly dispersed equiaxed pores (200 MPa at 5.3% strain) produced by HIP densification with NaCl powder space-holders [8]. This trend is in agreement with findings by Balla et al. [50], who used LENS to fabricate CP-Ti foams with orthogonal micro-channels aligned perpendicularly to the loading direction and who showed that their strength significantly exceeds that of foams with similar volume fractions of equiaxed porosity.

Sample LP with 24% porosity has a compressive strength of 600 MPa and strains up to 8.9% before failure (Fig. 5). Again, this is higher than the compressive strength of a 20% porosity martensitic foam (480 MPa) fabricated by HIP densification with NaF powder space-holders [49]. However, the latter deformed to ~15% before failure and had significant closed porosity that contributed to its low strength. The origin for the differences in mechanical properties is difficult to pinpoint, given the very different pore geometries, intensity of stress concentration near pores, and local changes in matrix chemical composition (due to Fe diffusion and TiC formation in the present samples).

4.5.2. Strain recovery

The percentages of plastic strain recovered upon heating after each cycle are high: 90–97% for sample LP and 89–94% for sample HP (Fig. 6), when ignoring the first loop with large relative error and the last loop with damage. The total strain recovered (from elastic, superelastic, and shape-memory contributions) for 6% applied strain is 94% for sample LP and 91% for sample HP. These values are very close to those recorded for NiTi foams with equiaxed porosity of similar volume fractions created by HIP densification with NaCl [8] and NaF [49] powder space-holders. Fig. 7 separates the maximum applied strain during each load cycle into plastic,

unloading recovery, and thermal (shape memory) recovery components. The residual plastic component remains low even at high applied strains of 6% for both samples. At low applied strains, both the elastic and superelastic components of the recovered strain are similar to the thermal component ε_{rec} , while at higher strains the thermal component becomes more dominant. Nonetheless, the present specimens can recover high amounts of strain elastically (1.2% for LP and 1.4% for HP) and superelastically (0.84% for LP and 0.95% for HP) on unloading. Their superelastic properties probably result from the Ni- and Fe-rich regions around the micro-channels in samples LP and HP, respectively.

The strain recovery behavior of the two samples is very similar despite their different pore fractions and compositions. This is explainable by the mechanical and geometrical similarities between the TiC in specimen LP and the non-transforming (Ni, Fe)Ti region in specimen HP, as both are non-transforming materials formed at comparable thicknesses around the channel wall. The total strain recovered by both specimens remains high despite the presence of these non-transforming phases, which agrees with previously published results on NiTi–TiC composites with high volume fractions of elastic TiC particles [66].

4.5.3. Stiffness

Fig. 8 shows the evolution of loading and unloading stiffness values during the cyclic compression tests for samples LP and HP. For both samples, the unloading stiffness values are higher than the loading stiffness values and increase with maximum applied strain. A similar trend has been documented for foams made by HIP densification with NaCl space-holders [8]. The unloading stiffness values reflect mostly elastic recovery, assuming superelasticity does not occur immediately upon unloading (the range used for calculating unloading stiffness being from $\sigma_{max} - 10$ MPa to $\sigma_{max} - 30$ MPa). On loading, however, both superelastic and plastic components of strains are present in the sample, so the measured stiffness is lower.

The stiffness values upon loading of sample HP (15–17 GPa) are similar to those of cortical bone (12–17 GPa [9]), making this porous NiTi material very suitable for bone implant applications. Sample LP, on the other hand, has higher loading stiffness values (22–26 GPa) which exceed those recorded for foams with 32–36% equiaxed porosity created by HIP densification with NaCl space-holders (4–6 GPa) [8]. It has been shown in CP-Ti that LENS-fabricated foams with elongated and orthogonal micro-channels aligned normal to the loading direction are stiffer than titanium with equiaxed pores [50]. Moreover, in the present NiTi foams, the elongated pores surrounded by a non-transforming, elastic region (TiC or (Ni, Fe)Ti) should produce lower stress concentrations than the blocky pores produced from NaCl powders, thus delaying the onset of detwinning.

5. Conclusions

Woven steel meshes are used as space-holders for the fabrication of nickel–titanium (NiTi) shape-memory alloys with interconnected micro-channels in a two-step process. First, NiTi powders are hot-pressed around stacks of space-holders to produce steel/NiTi composites. Second, removal of the steel is performed by electrochemical dissolution, resulting in stacked, two-dimensional networks of cylindrical micro-channels that replicated the original wire meshes. This method permits independent control over the volume fraction, size, morphology, and orientation of micro-channels created in NiTi.

Prior carburization of the meshes results in the formation of a thin TiC layer at the steel/NiTi interface during densification that lines the surfaces of the micro-channels after steel dissolution

and prevents the diffusion of iron into the NiTi matrix but also causes titanium depletion in the adjacent NiTi matrix. Without carburization, interdiffusion occurs between the steel and the NiTi, causing iron enrichment of the NiTi matrix near the micro-channels. In both cases, the transformation temperatures are decreased in the affected regions, which can thus become superelastic.

Two specimens with 24% and 34% open porosity were created with channel diameters of ~ 400 μm . They retain high compressive strengths and ductility as well as shape-memory recovery and partial superelastic recovery capabilities, while exhibiting low stiffness, comparable to that of cortical bone. These properties – combined with the biocompatibility of NiTi and the ability for the micro-channels to be osseointegrated – make these porous NiTi structures attractive for bone implant applications.

Acknowledgements

This research was supported by the National Science Foundation (NSF) through Grant DMR-0505772 and the Initiative for Sustainability and Energy at Northwestern (ISEN). A.J.N. also gratefully acknowledges the support of the Natural Sciences and Engineering Research Council of Canada (NSERC) through a Postgraduate Scholarship. The authors thank Dr. Bing Ye (Northwestern University) for his assistance with powder densification.

Appendix A. Figure with essential colour discrimination

Certain figure in this article, particularly Fig. 3, is difficult to interpret in black and white. The full colour images can be found in the on-line version, at doi:10.1016/j.actbio.2010.11.038.

References

- [1] Alvarez K, Nakajima H. Metallic scaffolds for bone regeneration. *Materials* 2009;2:790.
- [2] Navarro M, Michiardi A, Castano O, Planell JA. Biomaterials in orthopaedics. *J Royal Soc Interface* 2008;5:1137.
- [3] Geetha M, Singh AK, Asokamani R, Gogia AK. Ti based biomaterials, the ultimate choice for orthopaedic implants – a review. *Prog Mater Sci* 2009;54:397.
- [4] Bansiddhi A, Sargeant TD, Stupp SI, Dunand DC. Porous NiTi for bone implants: a review. *Acta Biomater* 2008;4:773.
- [5] Krishna BV, Xue WC, Bose S, Bandyopadhyay A. Engineered porous metals for implants. *Jom* 2008;60:45.
- [6] Rajagopalan S, Little AL, Bourke MAM, Vaidyanathan R. Elastic modulus of shape-memory NiTi from in situ neutron diffraction during macroscopic loading, instrumented indentation, and extensometry. *Appl Phys Lett* 2005;86:3.
- [7] Kim JS, Kang JH, Kang SB, Yoon KS, Kwon YS. Porous TiNi biomaterial by self-propagating high-temperature synthesis. *Adv Eng Mater* 2004;6:403.
- [8] Bansiddhi A, Dunand DC. Shape-memory NiTi foams produced by replication of NaCl space-holders. *Acta Biomater* 2008;4:1996.
- [9] Gibson LJ, Ashby MF. *Cellular solids: structure and properties*. Cambridge: Cambridge University Press; 1997.
- [10] Gupta HS, Seto J, Wagermaier W, Zaslansky P, Boesecke P, Fratzl P. Cooperative deformation of mineral and collagen in bone at the nanoscale. *Proc Natl Acad Sci* 2006;103:17741.
- [11] Thamburaja P, Anand L. Polycrystalline shape-memory materials: effect of crystallographic texture. *J Mech Phys Solids* 2001;49:709.
- [12] Panico M, Brinson LC. Computational modeling of porous shape memory alloys. *Int J Solids Struct* 2008;45:5613.
- [13] Otsuka K, Ren X. Physical metallurgy of Ti–Ni-based shape memory alloys. *Prog Mater Sci* 2005;50:511.
- [14] Lagoudas DC. *Shape memory alloys: modeling and engineering applications*. New York: Springer; 2008.
- [15] Pelton AR, Stockel D, Duerig TW. Medical uses of nitinol. In: Saburi T, editor. *Shape memory materials*, vols. 327–3. Zurich-Uetikon: Trans Tech Publications Ltd.; 2000. p. 63.
- [16] Yuan B, Zhang XP, Chung CY, Zeng MQ, Zhu M. A comparative study of the porous TiNi shape-memory alloys fabricated by three different processes. *Metall Mater Trans A – Phys Metall Mater Sci* 2006;37A:755.
- [17] Bertheville B. Porous single-phase NiTi processed under Ca reducing vapor for use as a bone graft substitute. *Biomaterials* 2006;27:1246.
- [18] Sadrnezhad SK, Arami H, Keivan H, Khalifezadeh R. Powder metallurgical fabrication and characterization of nanostructured porous NiTi shape-memory alloy. *Mater Manuf Process* 2006;21:727.

- [19] Sadrnezhaad SK, Hosseini SA. Fabrication of porous NiTi-shape memory alloy objects by partially hydrided titanium powder for biomedical applications. *Mater Des* 2009;30:4483.
- [20] Panigrahi BB, Godkhindi MM. Dilatometric sintering study of Ti–50Ni elemental powders. *Intermetallics* 2006;14:130.
- [21] Zhu SL, Yang XJ, Fu DH, Zhang LY, Li CY, Cui ZD. Stress-strain behavior of porous NiTi alloys prepared by powders sintering. *Mater Sci Eng A* 2005;408:264.
- [22] Zhu SL, Yang XJ, Hu F, Deng SH, Cui ZD. Processing of porous TiNi shape memory alloy from elemental powders by Ar-sintering. *Mater Lett* 2004;58:2369.
- [23] Grummon DS, Shaw JA, Gremillet A. Low-density open-cell foams in the NiTi system. *Appl Phys Lett* 2003;82:2727.
- [24] Zhao Y, Taya M, Kang YS, Kawasaki A. Compression behavior of porous NiTi shape memory alloy. *Acta Mater* 2005;53:337.
- [25] Hosseini SA, Sadrnezhaad SK, Ekrami A. Phase transformation behavior of porous NiTi alloy fabricated by powder metallurgical method. *Mater Sci Eng C* 2009;29:2203.
- [26] Bansiddhi A, Dunand DC. Processing of NiTi foams by transient liquid phase sintering. *J Mater Eng Perform*, in press.
- [27] Bansiddhi A, Dunand DC. Shape-memory NiTi–Nb foams. *J Mater Res* 2009;24:2107.
- [28] Lagoudas DC, Vandygriff EL. Processing and characterization of NiTi porous SMA by elevated pressure sintering. ASME/ASCE/SES joint summer meeting, San Diego, California; 2001. p. 837.
- [29] Greiner C, Oppenheimer SM, Dunand DC. High strength, low stiffness, porous NiTi with superelastic properties. *Acta Biomater* 2005;1:705.
- [30] Yuan B, Zhu M, Gao Y, Li X, Chung CY. Forming and control of pores by capsule-free hot isostatic pressing in NiTi shape memory alloys. *Smart Mater Struct* 2008;17:7.
- [31] Oppenheimer SM, Dunand DC. Porous NiTi by creep expansion of argon-filled pores. *Mater Sci Eng A* 2009;523:70.
- [32] Wisutmethagoon S, Denmud N, Sikong L. Characteristics and compressive properties of porous NiTi alloy synthesized by SHS technique. *Mater Sci Eng A – Struct Mater Prop Microstruct Process* 2009;515:93.
- [33] Tosun G, Ozler L, Kaya M, Orhan N. A study on microstructure and porosity of NiTi alloy implants produced by SHS. *J Alloy Compd* 2009;487:605.
- [34] Tay BY, Goh CW, Gu YW, Lim CS, Yong MS, Ho MK, et al. Porous NiTi fabricated by self-propagating high-temperature synthesis of elemental powders. *J Mater Process Technol* 2008;202:359.
- [35] Li BY, Rong LJ, Li YY, Gjunter VE. Synthesis of porous Ni–Ti shape-memory alloys by self-propagating high-temperature synthesis: reaction mechanism and anisotropy in pore structure. *Acta Mater* 2000;48:3895.
- [36] Bassani P, Giuliani P, Tuissi A, Zanotti C. Thermomechanical properties of porous NiTi alloy produced by SHS. *J Mater Eng Perform* 2009;18:594.
- [37] Yeh CL, Sung WY. Synthesis of NiTi intermetallics by self-propagating combustion. *J Alloy Compd* 2004;376:79.
- [38] Barrabés M, Sevilla P, Planell JA, Gil FJ. Mechanical properties of nickel–titanium foams for reconstructive orthopaedics. *Mater Sci Eng C* 2008;28:23.
- [39] Hu GX, Zhang LX, Fan YL, Li YH. Fabrication of high porous NiTi shape memory alloy by metal injection molding. *J Mater Process Technol* 2008;206:395.
- [40] Köhl M, Habijan T, Bram M, Buchkremer HP, Stöver D, Köller M. Powder metallurgical near-net-shape fabrication of porous NiTi shape memory alloys for use as long-term implants by the combination of the metal injection molding process with the space-holder technique. *Adv Eng Mater* 2009;11:959.
- [41] Krishna BV, Bose S, Bandyopadhyay A. Fabrication of porous NiTi shape memory alloy structures using laser engineered net shaping. *J Biomed Mater Res Part B* 2009;89:481.
- [42] Shishkovsky IV, Volova LT, Kuznetsov MV, Morozov YG, Parkin IP. Porous biocompatible implants and tissue scaffolds synthesized by selective laser sintering from Ti and NiTi. *J Mater Chem* 2008;18:1309.
- [43] Shishkovsky IV. Shape memory effect in porous volume NiTi articles fabricated by selective laser sintering. *Tech Phys Lett* 2005;31:186.
- [44] Li DS, Zhang YP, Ma X, Zhang XP. Space-holder engineered porous NiTi shape memory alloys with improved pore characteristics and mechanical properties. *J Alloy Compd* 2009;474:L1.
- [45] Wu S, Chung CY, Liu X, Chu PK, Ho JPY, Chu CL, et al. Pore formation mechanism and characterization of porous NiTi shape memory alloys synthesized by capsule-free hot isostatic pressing. *Acta Mater* 2007;55:3437.
- [46] Xiong JY, Li YC, Wang XJ, Hodgson PD, Wen CE. Titanium–nickel shape memory alloy foams for bone tissue engineering. *J Mech Behav Biomed Mater* 2008;1:269.
- [47] Aydogmus T, Bor S. Processing of porous TiNi alloys using magnesium as space holder. *J Alloy Compd* 2009;478:705.
- [48] Zhao X, Sun H, Lan L, Huang J, Zhang H, Wang Y. Pore structures of high-porosity NiTi alloys made from elemental powders with NaCl temporary space-holders. *Mater Lett* 2009;63:2402.
- [49] Bansiddhi A, Dunand DC. Shape-memory NiTi foams produced by solid-state replication with NaF. *Intermetallics* 2007;15:1612.
- [50] Balla VK, Bose S, Bandyopadhyay A. Understanding compressive deformation in porous titanium. *Phil Mag* 2010;90:3081.
- [51] Kwok PJ, Oppenheimer SM, Dunand DC. Porous titanium by electro-chemical dissolution of steel space-holders. *Adv Eng Mater* 2008;10:820.
- [52] Jorgensen DJ, Dunand DC. Ti–6Al–4V with micro- and macropores produced by powder sintering and electrochemical dissolution of steel wires. *Mater Sci Eng A* 2010;527:849.
- [53] Jorgensen DJ, Dunand DC. Structure and mechanical properties of Ti–6Al–4V with a replicated network of elongated pores. *Acta Mater* 2010;59:640.
- [54] Raghavan V. Fe–Ni–Ti (iron–nickel–titanium). *J Phase Equil Diff* 2010;31:186.
- [55] Ye B, Matsen MR, Dunand DC. Enhanced densification of Ti–6Al–4V powders by transformation-mismatch plasticity. *Acta Mater* 2010;58:3851.
- [56] Jackson CM, Wagner HJ, W RJ. 55-Nitinol – the alloy with a memory: its physical metallurgy, properties, and applications, vol. 42. Washington, DC: National Aeronautics and Space Administration; 1972.
- [57] Seifert HJ, Lukas HL, Petzow G. Thermodynamic optimization of the Ti–C system. *J Phase Equil* 1996;17:24.
- [58] Bozzolo G, Noebe RD, Mosca HO. Site preference of ternary alloying additions to NiTi: Fe, Pt, Pd, Au, Al, Cu, Zr and Hf. *J Alloy Compd* 2005;389:80.
- [59] Eckelmeyer KH. The effect of alloying on the shape memory phenomenon in nitinol. *Scr Metall* 1976;10:667.
- [60] Choi MS, Yamamoto T, Fukuda T, Kakeshita T, Taguchi E, Mori H. Differences between the R-phase and the commensurate phase in iron-doped Ti–Ni shape memory alloys. *Phil Mag* 2008;88:2449.
- [61] Airoldi G, Otsuka K, Riva G, Sciacca A, Zhang J. Differential scanning calorimetry study on transformations in a Ni4Ti50Fe3 alloy. *Mater Trans JIM* 1992;33:730.
- [62] Frenzel J, Zhang Z, Somsen C, Neuking K, Eggeler G. Influence of carbon on martensitic phase transformations in NiTi shape memory alloys. *Acta Mater* 2007;55:1331.
- [63] Otsuka K, Wayman CM. Shape memory materials. Cambridge: Cambridge University Press; 1998.
- [64] Sugiyama M, Hyun SK, Tane M, Nakajima H. Fabrication of lotus-type porous NiTi shape memory alloys using the continuous zone melting method and tensile property. *High Temp Mater Process (Lond)* 2007;26:297.
- [65] Brama M, Rhodes N, Hunt J, Ricci A, Teghli R, Migliaccio S, et al. Effect of titanium carbide coating on the osseointegration response in vitro and in vivo. *Biomaterials* 2007;28:595.
- [66] Vaidyanathan R, Bourke MAM, Dunand DC. Phase fraction, texture and strain evolution in superelastic NiTi and NiTi–TiC composites investigated by neutron diffraction. *Acta Mater* 1999;47:3353.
- [67] Fukami-Ushiro KL, Dunand DC. NiTi and NiTi–TiC composites. 3. Shape-memory recovery. *Metall Mater Trans A – Phys Metall Mater Sci* 1996;27:193.
- [68] Buser D, Schenk RK, Steinemann S, Fiorellini JP, Fox CH, Stich H. Influence of surface characteristics on bone integration of titanium implants – a histomorphometric study in miniature pigs. *J Biomed Mater Res* 1991;25:889.
- [69] Martin JY, Schwartz Z, Hummert TW, Schraub DM, Simpson J, Landkoff J, et al. Effect of titanium surface roughness on proliferation, differentiation, and protein synthesis of human osteoblast-like cells (MG63). *J Biomed Mater Res* 1995;29:389.
- [70] Perez LM, Gracia-Villa L, Puertolas JA, Arruebo M, Irusta S, Santamaria J. Effect of nitinol surface treatments on its physico-chemical properties. *J Biomed Mater Res Part B* 2009;91:337.
- [71] Shabalovskaya S, Anderegg J, Van Humbeeck J. Critical overview of Nitinol surfaces and their modifications for medical applications. *Acta Biomater* 2008;4:447.
- [72] Likibi F, Chabot G, Assad M, Rivard CH. Influence of orthopedic implant structure on adjacent bone density and on stability. *Am J Orthoped* 2008;37:E78.
- [73] Assad M, Chernyshov A, Leroux MA, Rivard CH. A new porous titanium–nickel alloy: part 2. Sensitization, irritation and acute systemic toxicity evaluation. *Biomed Mater Eng* 2002;12:339.
- [74] Assad M, Chernyshov AV, Jarzem P, Leroux MA, Coillard C, Charette S, et al. Porous titanium–nickel for intervertebral fusion in a sheep model: part 2. Surface analysis and nickel release assessment. *J Biomed Mater Res Part B* 2003;64:121.
- [75] Assad M, Chernyshov A, Leroux MA, Rivard CH. A new porous titanium–nickel alloy: part 1. Cytotoxicity and genotoxicity evaluation. *Biomed. Mater. Eng.* 2002;12:225.
- [76] Assad M, Jarzem P, Leroux MA, Coillard C, Chernyshov AV, Charette S, et al. Porous titanium–nickel for intervertebral fusion in a sheep model: part 1. Histomorphometric and radiological analysis. *J Biomed Mater Res Part B* 2003;64:107.
- [77] Ayers RA, Simske SJ, Bateman TA, Petkus A, Sachdeva RLC, Gyunter VE. Effect of nitinol implant porosity on cranial bone ingrowth and apposition after 6 weeks. *J Biomed Mater Res* 1999;45:42.
- [78] Kujala S, Ryhänen J, Danilov A, Tuukkanen J. Effect of porosity on the osteointegration and bone ingrowth of a weight-bearing nickel–titanium bone graft substitute. *Biomaterials* 2003;24:4691.
- [79] Frenzel J, Pftizing J, Neuking K, Eggeler G. On the influence of thermomechanical treatments on the microstructure and phase transformation behavior of Ni–Ti–Fe shape memory alloys. *Mater Sci Eng A* 2008;481–482:635.
- [80] Frenzel J, George EP, Dlouhy A, Somsen C, Wagner MFX, Eggeler G. Influence of Ni on martensitic phase transformations in NiTi shape memory alloys. *Acta Mater* 2010;58:3444.